Eddy Asymmetry in the Sheared Heated Boundary Layer

L. MAHRT

Oregon State University, Corvallis, Oregon

(Manuscript received 8 March 1990, in final form 24 August 1990)

ABSTRACT

Statistical measures are developed to study the influence of mean shear on the asymmetry of eddy updrafts as observed from low-level aircraft flights in HAPEX, FIFE, and SESAME. This asymmetry involves formation of microfronts between updrafts with slow horizontal motion and downdrafts with faster horizontal motion. The variance of the Haar-wavelet transform (step-function basis) is found to be a superior indicator of the dominant scales of such eddies compared to the structure function. For those analyses where scale dependence is not of interest, the simpler structure function is applied. The coherent structures at the dominant scale are examined by computing eigenvectors of the lagged correlation matrix based on conditionally sampled events.

With strong mean shear and weak surface heating, the horizontal motion field of the main coherent eddies is more in phase with the vertical motion which corresponds to efficient vertical transport of horizontal momentum. With stronger heating and weaker mean shear, the horizontal convergence beginning at the microfront extends inward across the updraft. Consequently, the decorrelation between fluctuations of horizontal and vertical velocity components in the heated boundary layer results from a systematic phase difference rather than randomness of the horizontal velocity fluctuations as proposed in previous studies. This phase difference leads to decreasing Prandtl number with increasing convective instability. This conceptual model of the main eddies is used to interpret the variation of other statistics of fluctuating gradients between different types of atmospheric turbulence.

1. Introduction

Vertical transport in the lower part of the heated boundary layer is organized by buoyant updrafts. With mean vertical shear, the updrafts become asymmetric with horizontal convergence and sharp horizontal changes of temperature and moisture at the upstream edges of the updrafts (Kaimal and Businger 1970: see also Fig. 6a of section 4 below).

The formation of concentrated zones of horizontal gradients at the upstream edges of the updrafts also occurs with shear-driven updrafts in the surface layer (Schols 1984), wind gusts penetrating into the forest canopy (Shaw et al. 1990), updrafts penetrating into faster moving ambient flow at the boundary-layer top (Mahrt 1981), and occurs with the relative horizontal motion of the up- and downdrafts in clear-air turbulence (Mahrt and Frank 1988). The essential ingredient appears to be horizontal convergence induced by eddy vertical advection in the presence of mean vertical shear. Near the surface, this horizontal convergence occurs between downdrafts with stronger horizontal flow and updrafts with weaker horizontal motion. The relation of horizontal asymmetry of updrafts in the boundary layer to the mean shear and surface heating, and the influence of this asymmetry on momentum transport is the main subject of this study.

For convenience, the zones of concentrated spatial changes at the convergent upstream edges of the updrafts are referred to as microfronts. Atmospheric studies of microfronts include Kaimal and Businger (1970), Wilczak (1984), Stull (1988, sections 11. 1.2–3), and Shaw et al. (1990). Observational studies of microfronts in turbulent laboratory flows are cited in the Introduction of Mahrt (1989). The signature of the asymmetric eddies and upstream microfronts in time series are often idealized as ramp structures (e.g., Antonia and Atkinson 1976). Ramp structures associated with larger eddies above the surface layer may be related to the convergence zones observed by Doppler radar (see Stull 1988, p. 446 for examples).

At the divergent downstream edges of updrafts, the horizontal gradients are more diffuse and might correspond to a wake resulting from the motion of the faster moving ambient flow around the updraft. This horizontal asymmetry of the updrafts causes a sign preference for the strongest gradients as can be measured by the skewness of the horizontal gradients. The mean shear also leads to elongation of the updrafts in the direction of the mean shear (Lenschow 1970; Nicholls 1978; Wilczak and Tillman 1980; Grossman 1982). This elongation leads to larger horizontal length scale of the main eddies when observed along the direction of the mean shear.

Corresponding author address: Dr. Larry Mahrt, Dept. Atmospheric Sciences, Oregon State University, Corvallis, Oregon 97331-2209.

The formation of microfronts contributes significantly to the total turbulent flux as demonstrated in the studies of Antonia and Chambers (1978), Schols (1984), Chen and Blackwelder (1978), Kikuchi and Chiba (1985), and Gao et al. (1989). In the study of Bergström and Högström (1989) the microfronts and parent ramp structures accounted for about 90% of the flux above a pine forest even though such structures represent less than half of the record. The microfronts may also provide a more direct link between the main eddies and dissipation because the concentrated gradients at the edges of the main eddies can contribute directly to the dissipation without a sequence of instabilities and gradual cascade of energy to smaller and smaller scales. The importance of this short circuit of the energy cascade is not known.

The present study examines the influence of vertical mean shear on the asymmetry of drafts in different boundary layers with a range of surface heating rates and mean shear values. Toward these goals, measures of the asymmetry of the main coherent structures have been developed which are then computed from 61 different aircraft legs from 3 major field programs (Table 1). The particular measures of asymmetry are motivated in the next section along with consideration of sampling problems.

2. Statistical measures

The asymmetry of the main events and associated sharp edges will be studied by locally transforming the original data $f(x)$ to estimate spatial differences as a function of scale. The techniques presented in this section will be applied in sections 4–6 to study sheared updrafts and associated microfronts, where $f(x)$ will represent the three velocity components, temperature or moisture and x represents position within the aircraft record.

When events in the time series are not periodically positioned, local transforms are better able to identify the main scale of the events as compared to global decompositions such as the usual Fourier transform. To illustrate the difference between global and local transforms, two orthogonal scales of the Walsh global basis set are plotted in Fig. 1a along with two orthogonal scales of the local Haar basis set (Fig. 1b) where at a given scale, each local basis is spatially orthogonal because of zero overlap. Fig. 1c sketches loss of orthogonality at a given scale due to spatial overlap of the local transforms (oversampling).

The local transform is computed as the integral of the local basis function with the original data as outlined in the following. The notation, terminology, and mathematical development will be simplified as much as possible with an attempt to be consistent with wavelet transform theory (Daubechies 1988). The local transform of the data $W\{f(x), a, b\}$ will be defined over a window of width a (Fig. 2). The dilation scale of the basis set and the width of the transformation window of local integration are numerically the same in this particular study, and the usual distinction between the two is not needed. The location of the window center within the record is $x = b$ and b_0 is the incremental translation of the window position between calculations of the local transform (Fig. 1c).

The transformation operator $W\{f(x), a, b\}$ for estimating spatial differences can be expressed in the form:

$$W\{f(x), a, b\} = a^{-1} \int h[(x-b)/a] f(x) dx \quad (1)$$

where the integration is over the transformation window of width $a > 0$ and again b is the translate (centering of the local transform). Equation (1) is equivalent to the usual form of the wavelet transform (Daubechies 1988) where the integral (1) is normalized by $a^{-1/2}$ instead of a^{-1} and the basis function is normalized by $a^{-1/2}$, whereas no normalization is applied here. In order to estimate the spatial change of $f(x)$ across the window, the basis function $h[(x-b)/a]$ will be defined in terms of the Haar basis (step function, Fig. 2) as in Daubechies (1988), Mahrt and Frank (1988), and others. For comparison with previous turbulence studies, the basis function will also be posed in terms of a two point differencing operator (structure function). Since the principal purpose will be to assess the scale of maximum activity rather than efficient decomposition of the data, the transforms used here will be neither orthogonal with respect to different scales (dilations) nor spatially orthogonal so that transformation windows at a given scale may overlap.

With application to actual data, (1) must be defined in discrete form in which case (1) becomes a discrete sum over the K observational points in the window of width $a = (K-1)\Delta x_{\min}$ where $\Delta x_{\min}$ is the resolution or sampling interval of the data. To compute the above measure of spatial change as a function of position within the record, this window marches through the record by sequentially moving the window's position "b" by some translation increment of $b_0/\Delta x_{\min}$ points.

a. *Haar-wavelet transform for spatial differences*

The Haar-basis function (Fig. 2) can be written in the form:

$$h[(x-b)/a] = \begin{cases} -1 & \text{for } -\frac{1}{2} < (x-b)/a < 0 \\ +1 & \text{for } 0 < (x-b)/a < \frac{1}{2} \\ 0 & \text{otherwise.} \end{cases} \quad (2)$$

The wavelet transform is computed by substituting (2) into (1). The Haar-basis function satisfies the admissibility condition for wavelet theory (Grossmann et al. 1989) but is discontinuous and does not satisfy con-

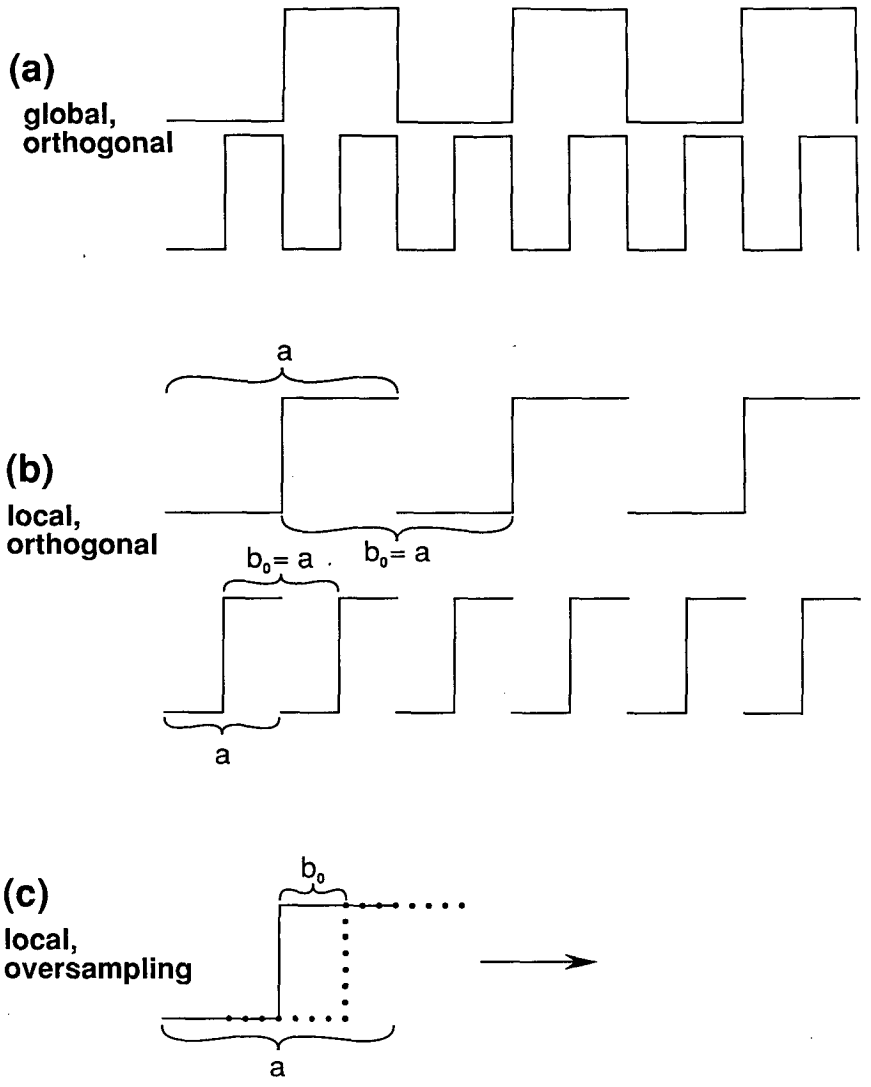

FIG. 1. Examples of (a) two adjacent scales of the Walsh global orthogonal basis set, (b) two adjacent scales of the Haar local orthogonal basis where, for a given scale, spatial orthogonality between different bases results from spatial nonoverlap, and (c) loss of orthogonality of a local basis set due to spatial overlap between bases. In this sketch, the basis amplitudes are arbitrary.

tinuity requirements for stricter definitions of wavelet transforms (e.g., Meyer 1989). This distinction becomes less important in the present application to discrete data.

Substitution of the Haar basis (2) into the wavelet transform verifies that this version of the wavelet transform (1) preserves energy. Specifically, the transform of itself is unity

$$a^{-1}\int \{h[(x-b)/a]\}^2 dx = 1.$$

Similarly, the wavelet transform of a structure with the same shape as the Haar-basis function $h[(x-b)/a]$, but of amplitude A (varying from $+A$ to $-A$) is simply A or one-half of the difference of this structure between the two halves of the transform.

In general, the Haar-wavelet transform can be written as one-half of the difference between the average values of $f(x)$ for each of the two halves of the trans-

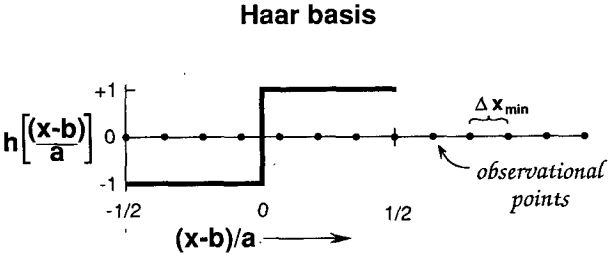

FIG. 2 Sketch of one Haar-basis function superimposed on the time series.

formation window. Since the two averages are centered at $(x - b)/a = +a/4$ and $-a/4$, the corresponding gradient can be constructed by dividing the difference of averages by $a/2$.

The Haar-wavelet transform of a sudden change in the record is largest at the dilation scale which corresponds to the scale of the "coherency" or "width of influence" of the change rather than to the width of the change itself. For example, for an artificial record containing top hats, the Haar-wavelet transform is maximum at the dilation corresponding to the twice the width of the top hats where one of the two arms of the Haar-basis function coincides with the width of the top hat. With the top hat data, the width of the transition zone containing the change is zero; that is, the change is discontinuous. For the case of an updraft with an upstream microfront edge, the wavelet transform is largest for a window width comparable to twice the width of the updraft in contrast to the much smaller width of the microfront zone. For comparison, the energy peak of the Fourier transform occurs at the scale of the periodicity which includes the spacing between the updrafts. Inference of the main eddy scale from Fourier spectra is ambiguous for the data analyzed in this study partly because the updraft events are not very periodic.

To further study this scale dependence, consider the short interval of aircraft-measured vertical velocity plotted in the upper part of Fig. 3. The corresponding phase plot of the wavelet transform as a function of dilation scale (vertical axis) and position in the record (horizontal axis) is constructed at the bottom of Fig. 3. See Argoul et al. (1989) for an example of such a phase plot for laboratory turbulence. The largest values of the wavelet transform in Fig. 3 tend to occur at dilation scales of roughly 500–600 m as will be quantitatively documented later in this study. This dilation corresponds roughly to the width of the most organized updraft–downdraft pairs and not the scale of the much narrower microfront transition zones occurring on a scale of a few tens of meters in Fig. 3. The spatial locations of the maximum values of the wavelet transform for a fixed dilation of $a = 500$ m (Fig. 3, middle) occurs where the transformation window is centered at the microfronts. Fig. 3 also underscores the complexity of turbulence data on a variety of scales, and an objective method is needed to statistically quantify the dependence of the wavelet transform on dilation.

In fact, a principal goal of this study is to determine the scale of maximum activity or main event size for the record as a whole. Instead of incorporating the usual application of the wavelet transform, this study will examine the statistics of the wavelet-transformed variable $W\{f(x), a, b\}$ averaged over the entire record as a function of dilation scale a. For example, summing the squares of the wavelet transform over the record separately for different dilation scales provides a "wavelet variance spectra" whose peak is a measure of

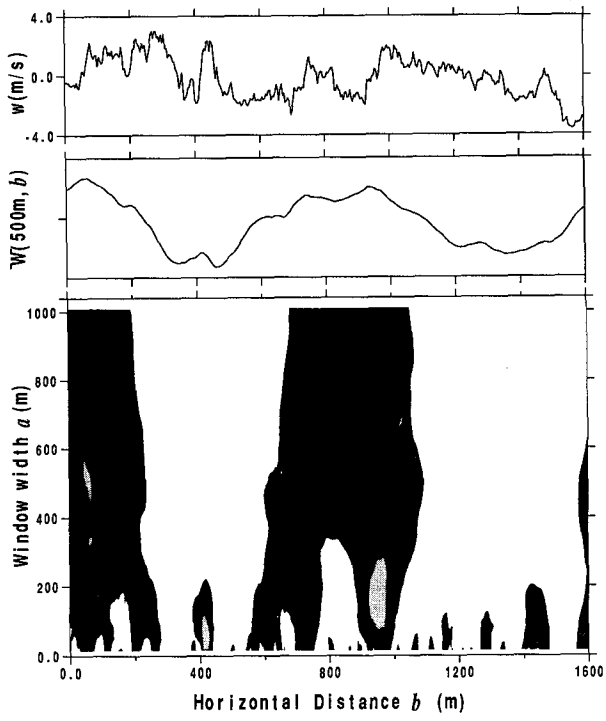

FIG. 3. Identification of concentrated horizontal changes from the Haar-wavelet transform. The upper diagram is the raw time series with the downstream distance to the right, the middle diagram is the Haar-wavelet transformed time series with a window width of 500 m while the bottom phase plot of the Haar-wavelet transform represents the transformed values for various window widths a (vertical coordinate) as a function of horizontal distance in the downstream direction b. Horizontal hatching indicates strongest horizontal changes of positive sign, dark shading weaker positive changes, white areas weak negative horizontal changes, and vertical hatching shows the regions of strongest negative horizontal changes.

the scale of dominant event size. This expectation is based on wavelet transforms of artificial records with various shaped events and various levels of noise (to be reported elsewhere).

To allow statistics for arbitrary moments of the wavelet transform, (1) is rewritten so that the order of the moment appears explicitly by defining

$$D^p(a) = [(W\{f(x), a, b\})^p] \qquad (3a)$$

where the outer square brackets represent a simple unweighted average of the moment of the wavelet transform over all of the local transforms of the record for a given scale a. In discrete form, (3a) can be written as

$$(1/N) \sum (h[(x - b_n)/a] f(x))^p \qquad (3b)$$

where b_n are the N different positions of the transformation window as it sequentially marches through the record, usually one point at a time (maximum oversampling). Relationship (3b) will be used to compute the wavelet variance ($p = 2$) and to form the deter-

mination of wavelet skewness discussed in subsection c and applied to aircraft data in section 4.

b. Wavelet representation of the structure function

The structure function based on two-point differences is the simplest and most direct measure of spatial variations on different scales, and has been a traditional statistical tool in the study of turbulence. It also appears to be less vulnerable to sampling problems compared to Fourier decomposition (Lumley and Panofsky 1964; Babiano et al. 1985; Mahrt and Gamage 1987). For cosmetic uniformity, the calculation of the structure function can be posed in the "format" of the wavelet transform where the differencing operator becomes

$$h[(x-b)/a] = \begin{cases} -1, & \text{for } (x-b)/a = -\frac{1}{4} \\ 1, & \text{for } (x-b)/a = \frac{1}{4} \\ 0, & \text{for all other } x. \end{cases} \quad (4)$$

This basis function operates on data as in (1) except that scaling with respect to dilation scale a in (1) is omitted. The resulting transformed variable $W\{f(x)\}$ is simply the difference of $f(x)$ across the "separation distance" $r = a/2$. In contrast, the Haar-wavelet transform computes average values for each of the window halves and then computes the difference. To be consistent with respective conventions, the structure function will be posed in terms of separation distance and the wavelet transform in terms of window width (dilation). The structure basis function (4) has zero mean but does not possess needed continuity properties and admissibility conditions for wavelet theory as defined in Grossmann et al. (1989). It is used here because of its simplicity and extensive use in previous turbulence studies.

To compute the structure function variance for the record, the structure difference operator (4) is substituted into (3b) for $p = 2$. The relationship between the structure function and the Haar-wavelet transform for a given window width can be constructed by defining

$$f(x) = [f(x)]_j + f'(x) \quad (5)$$

where the square brackets indicate averaging over each of two halves of the transformation window, each of width $a/2$ corresponding to the two parts of the Haar basis function (Fig. 2), the subscript $j = 1$ refers to the first window half where $h[(x - b_n)/a] = -1$ and $j = 2$ refers to the second window half where $h[(x - b_n)/a] = +1$. The quantity $f'(x)$ is the deviation of $f(x)$ from the respective half window average. Using decomposition (5) and computing the structure difference (4) over separation distance $r = a/2$ and squaring for each of the $K/2$ possible calculations of (4) within the window, the structure variance in the transformation window becomes

$$(2/K) \sum \{[f(x)]_2 + f'(x_{(K/2)+k}) - [f(x)]_1 - f'(x_k)\}^2 \quad (6)$$

where K is the number of points in the window. The sum in (6) is defined from $k = 1, K/2$ to incrementally move the structure differencing operator through the transformation window of width a.

Noting that $[f(x)]_2 - [f(x)]_1$ is simply twice the Haar-wavelet transform $W\{f(x), a, b\}$ and noting that $f'(x)$ vanishes when summed over each window half, the structure function eventually reduces to

$$4W^2\{f(x), a, b\} + (2/K) \sum \{f'(x_k) - f'(x_{(K/2)+k})\}^2. \quad (7)$$

Consequently, the structure function averaged over the window of width a is the sum of a contribution proportional to the wavelet variance plus an additional small-scale contribution. The structure variance approaches the wavelet variance within a scaling factor when the smaller-scale variation completely vanishes. The smaller-scale contribution always increases the value of the structure function. The small-scale contribution results from the fact that the calculation of the structure function corresponds to squaring of the difference *before* averaging whereas application of the wavelet transformation averages before computing the difference.

Since scales larger than the window width are at least partially removed and the built-in averaging of the Haar-wavelet transform removes smaller scales, the Haar-wavelet transform acts as a band-pass filter and is therefore more focused on a given scale. In contrast, the structure function "accumulates" variance with increasing separation distance and is more analogous to a high-pass filter. Because of leakage of variance from smaller to larger separation distances, the value of the structure function in geophysical examples tends to increase indefinitely with scale whereas the Haar-wavelet transform tends to peak at the main event scale, as will be seen in section 5. Therefore, the Haar-wavelet transform appears to be more useful than the structure function for isolating the scale of the dominant events. However, the simpler and more traditional structure function will still be used when comparing the gradient variance between different flows at a fixed separation distance. For such a fixed scale, the scale ambiguity of the structure function is not so serious.

c. Wavelet skewness and kurtosis

A generalized dimensionless function for studying the sign preference and intermittency of gradients can

be defined in terms of the higher moments of the wavelet transform (3)

$$G^p(L') = D^p(a)/\{D^2(a)\}^{p/2} \quad (8)$$

where this ratio becomes the dimensionless Haar-wavelet transform when based on (2) and becomes the dimensionless structure function (e.g., Frisch et al. 1978) when the transform is based on (4). Note that the nondimensional ratio (8) is the same for differences and gradients since the division by the window width or separation distance required to convert differences to gradients cancels in (8). For example, with $p = 3$, (8) becomes the skewness of gradients which measures the sign preference for strong horizontal gradients which is significant in turbulent eddies in sheared flows. As a numerical example, the scale dependence of the skewness and kurtosis for the structure function of artificial records consisting of ramp functions or top hats can be computed from Eq. (2.12) in Van Atta (1977), Eq. (2) in Antonia et al. (1982) and Eq. (16) of Mahrt (1989).

The skewness and kurtosis of the structure function and Haar-wavelet transform describe features of the strongest spatial differences. This is quite different from the skewness and kurtosis of deviations from a local mean (centered differencing) as might be constructed from high pass filtered data. For example, in buoyancy driven turbulence updrafts with little mean shear would be characterized by large positive skewness of deviations of vertical velocity and temperature from the local mean but small skewness of spatial gradients. On the other hand, strongly sheared updrafts are characterized by smaller skewness of deviations from the mean values but larger skewness of gradients due to shear-induced asymmetry.

Unfortunately, sampling problems affect the calculation of higher moments more than variances (Tennekes and Wyngaard 1972). Furthermore, nondimensional higher moments such as skewness and kurtosis can be systematically augmented by inhomogeneity common in geophysical records (Mahrt 1989). As a result of such sampling problems, the skewness analysis in this study will be based primarily on the longest aircraft records.

d. Selection of samples and decomposition into eigenvectors

To study the structure of the main events, samples of the events will be selected and decomposed into eigenvectors of the sample-lagged covariance matrix according to the overall strategy sketched in Fig. 4. The sample width, L', is chosen to be the dilation scale corresponding to the approximate peak of the wavelet variance spectra. To select the samples, a transformation window of width L' incrementally marches through the record and computes the Haar-wavelet transform for vertical velocity at each point in the record as in Mahrt and Frank (1988). When the Haar-wavelet transform at a point exceeds the value of its standard deviation for the record and is the largest value in the surrounding neighborhood of width L', then a sample of width L' is selected, centered at that point in the record; that is, samples with centered, concentrated, horizontal changes are selected with no overlap between samples. Additional sampling restrictions may be imposed on the sign of the wavelet transform based on the skewness of the wavelet transform or based on the physics of the problem. For example, in section 6 only those samples which agree with the sign expected from shear-induced asymmetry of updrafts are selected.

The next step is to find prototype structures that define the main features of the samples and provide a new basis set upon which the samples can be projected. While the composite structure computed by averaging all of the samples is of interest, it is often misleading since the samples may contain different types of structures and the average structure may not be similar to any of the samples. As an alternative, the eigenvectors of the sample lagged correlation matrix are computed as applied in Lumley (1970), Busch and Petersen (1971), Petersen (1976), Panofsky and Dutton (1984), and Mahrt and Frank (1988). See Sirovich (1987) for a more general point of view with alternate computational techniques. The eigenvectors are determined by maximizing the covariance explained for the selected samples and thus form a natural basis set for the samples, which also seems to facilitate physical interpretation.

However, the eigenvector calculations are vulnerable to sampling problems. Therefore in section 6, the eigenvector analysis is confined to only those datasets with total record length greater than 100 km over relatively homogeneous terrain. For this analysis, the observational vector representing a given sample is "stacked" (Petersen 1976; Mahrt and Frank 1988) with the three velocity components and temperature to study the spatial structure associated with covariance between the temperature and velocity components.

3. The data and physical regimes

a. The field programs

The most important dataset for this study consists of six horizontal legs approximately 120 km long and approximately 150 m above a nearly flat artificial pine forest in southwest France on each of two fair weather days, 19 and 25 May (Table 1) during the Hydrological and Atmospheric Pilot Experiment (HAPEX, André et al. 1988; Pinty et al. 1989; Noilhan and Planton 1989). These two days are characterized by significant surface heating and modest winds with a speed of 3–4 m s^{-1}. The statistics for these two days vary little between flight legs probably because:

1) these data contain one of the largest sample sizes

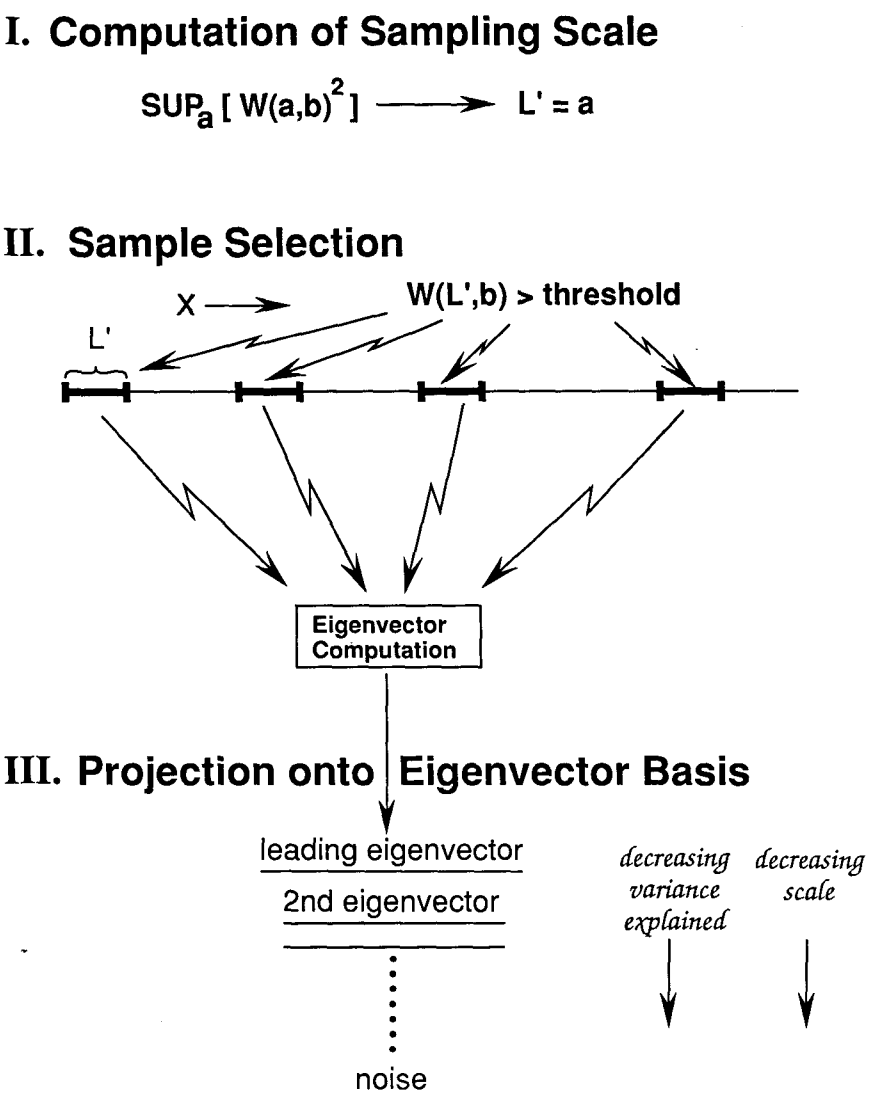

FIG. 4. Schematic summary of strategy outlined in section 2d where the peak of the wavelet variance spectra (step I) provides the selected dilation (window width). The square brackets correspond to averaging the variance of the wavelet transform over the record for a fixed value of the dilation a. The selected width L' is then used to extract samples based on positions of local maximum values of wavelet transform (step II). Samples are then decomposed into eigenvectors of the sample-lagged covariance matrix (step III).

accumulated by low-level aircraft flights over land with approximately stationary conditions,

2) the inhomogeneity is limited mainly to occasional clearings in the pine forest. The forest consists primarily of one specie of pine, albeit of varying tree height, with some variation of the understory vegetation. The soil type is sandy and relatively uniform.

As a result, the sampling problems for skewness and kurtosis briefly discussed in section 2 are minimal for these two days. The remaining datasets used here are affected by some sampling problems which lead to scatter in the subsequent diagrams but do not destroy the overall relationship between variables. Four additional days are included from HAPEX with shorter flight legs (Table 1) over forest and mixed farmland on each day (see André et al. 1988).

A second dataset consists of six low-level east–west flights above the Konza Prairie in Kansas, carried out during FIFE (First ISLSCP Field Experiment, Sellers et al. 1988). Here, the 100-m wind is 11–12 m s^{-1} from the south–southwest so that most of the strong shear is directed perpendicular to the flight path. However, because of the strength of the airflow, the shear parallel to the flight path is still significant. On this day, the surface evapotranspiration is quite large leading to only modest surface heating.

A third dataset was collected during a fair weather

period of the Severe Environmental Storms and Mesoscale Experiment (SESAME). This dataset consists of nocturnal intermittent turbulence occurring at the top of a very stable, nonturbulent, surface inversion layer on 5 May 1979 (Mahrt 1985) and continuous turbulence in a windy nocturnal boundary layer occurring on 6 May (Lenschow et al. 1988).

Analysis of sampling problems indicate that fluxes are least reliable for the 5 SESAME case where the turbulence is intermittent and record lengths are short. Fluxes are most reliable for 19 and 25 HAPEX which contain long records over relatively homogeneous terrain. Two of the flight legs on 19 June HAPEX are characterized by small momentum fluxes which are probably characterized by significant sampling problems. They lead to "off-scale" values of the stability parameter (Table 2) and therefore are not included in the figures.

b. *Preliminary classification of days*

The present datasets include a range of heat flux and mean shear values. A rough classification can be expressed in terms of the bulk instability $-h/L$ (Table 2) where h is the boundary-layer depth and L is the Obukhov length based on the filtered fluxes. In this study, fluctuations are computed using a 2-pole high-pass Tangent–Butterworth filter with a 5-km wavelength for all of the datasets except SESAME 5 May (500-m wavelength) and 6 May (1-km wavelength). On these two days, the turbulence is smaller scale and the record lengths are shorter. The filter cutoff lengths are based on cospectra of temperature and vertical velocity. Filtering is used only in the calculation of fluxes while the structure function and wavelet transform are applied to raw data.

In unstable cases, the vertical velocities are relatively large due to buoyancy generation of vertical momentum and weaker in stable cases due to the constraining influence of buoyancy effects. As a measure of the relative strength of the horizontal gradients of vertical velocity, the velocity aspect ratio is computed based on the structure function

$$A(r) = 2D_w^2(r)/[D_u^2(r) + D_v^2(r)]. \quad (9)$$

Figure 5 shows the expected increase of the velocity aspect ratio with increasing instability for an arbitrary separation distance of $r = 75$ m. The dependence on stability is not sensitive to the choice of r at least for the present data. For the HAPEX cases where surface heating is quite significant, the variance of the vertical velocity gradients exceeds that of the gradients of the horizontal velocity components, as measured by (9). For the FIFE and SESAME cases, the vertical velocity gradients are roughly half of the horizontal components indicating that the buoyancy production of turbulence is secondary in the FIFE case while buoyancy acts to reduce turbulence vertical motions in the stable SESAME cases. As expected, scatter is greatest for SESAME 5 May and some of the HAPEX days with shorter flight legs over inhomogeneous surfaces.

4. Gradient skewness and relation to shear

a. *Structure skewness*

The structure skewness responds to the preferred sign of the sharpest gradients as depicted in the plausible geometry of Fig. 6a. The statistics of gradients will be interpreted in terms of such a conceptual model but it must be realized that such statistics represent a variety of influences. For example, the observed structure skewness is also related to the orientation of the flight direction with respect to the mean shear vector. *The longitudinal direction* will be referred to as the direction of the mean shear projected onto the flight path (Fig. 6b). For the present data where the mean wind and wind shear are roughly the same direction, the *longitudinal component* is the wind vector projected onto the flight path. The *lateral component* is defined to be the wind component perpendicular to the flight path

TABLE 1. Field programs.

Program	Number	Length (km)	Height (m)	Direction	Location	Weather
HAPEX						
19 May	6	120	125	EW	Flat pine forest	Cu < 10%
25 May	6	120	160	EW	Flat pine forest	Cu < 10%
13 June	7	40	100	S	Rolling, mixed	10% Cu, windy
19 June	8	40	100	S	Rolling, mixed	Clear
22 June	9	40	100	S	Rolling, mixed	<10% Cu, windy
1 July	10	40	100	S	Rolling, mixed	Vble Sc
FIFE						
6 June	6	30	125	EW	Hilly grassland Konza Prairie	Clear, windy
SESAME						
5 May	4	16	50	NS	Rolling grassland Oklahoma	Clear
6 May	4	13	30	NS	Rolling grassland Oklahoma	Clear

(Fig. 6b). This convention is different from the usual tower coordinate system where the longitudinal direction is completely aligned with the mean wind vector.

With the coordinate system used here, dominance of the skewness of small-scale horizontal gradients by microfronts corresponds to negative skewness of the longitudinal flow (horizontal convergence) and positive skewness of temperature, moisture, and vertical velocity; that is, the microfronts correspond to transitions from sinking, cool, dry air to rising, warm, moist air across the microfront in the direction of mean horizontal flow (Fig. 6a). The observed skewnesses tend to be consistent with the microfront conceptual model (Table 2).[1]

The microfront model fails to systematically predict the signs of the skewnesses in cases with very weak winds in the flight direction, and in cases with stable stratification (SESAME). For the remaining cases, the microfront model predicts the sign of the structure skewness for the longitudinal velocity in all cases except one. The prediction for temperature is relatively good, the prediction for vertical motion is good only with the long flights over relatively homogeneous terrain (19 May and 25 May), and the prediction for moisture is even less systematic. The statistics of moisture variations near the surface are sometimes strongly influenced by especially dry air originating from downdrafts (Mahrt 1991).

The structure variance of the two normal velocity components (vertical and lateral components) represent components of the shear tensor in contrast to the structure of the longitudinal component which represents convergence. The *skewness* of the gradients of the vertical and lateral velocity components are *less than* that of the longitudinal (along-flight) component (Table 2), while the structure *variance and kurtosis* for the vertical and lateral velocity components are *greater* than that for the longitudinal component. The sign preference of the convergence and corresponding gradient *skewness* of the longitudinal velocity component is consistent with the preferential augmentation of horizontal convergence at the microfronts. On the other hand, the *magnitude* of the longitudinal velocity gradient is limited by pressure effects which apparently lead to smaller structure variance compared to that for the other two velocity components. This possibility is now discussed in more detail.

TABLE 2. The bulk stability ($-h/L$), mean wind direction, mean horizontal velocity components in the usual Cartesian coordinates (m s^{-1}), averaged vertical fluxes based on high-pass filtered data (5-km cutoff wavelength) for the horizontal wind components (m^2 s^{-2}), moisture (m s^{-1} g kg^{-1}) and virtual temperature (m s^{-1} °K) and the kurtosis and skewness of the structure function (see text).

					High-pass flux				Structure kurtosis				Skewness			
Data set	$-h/L$	Dir.	U	V	WU	WV	Wq	WTH_v	U	V	W	Q	T	Long.	W	T	Q
SESAME 05 May 79	−27.10	S	5.06	−0.79	0.0000	−0.0001		−0.0001	9.09	9.94	5.11		9.61	0.14	0.01	0.18	
	−1.08	S	2.85	−0.60	−0.0019	0.0000		−0.0004	8.25	8.74	6.71		15.37	0.11	−0.05	1.36	
	−1.46	N	1.27	−1.01	−0.0043	0.0001		−0.0017	8.18	9.87	12.52		13.11	−0.15	0.13	0.33	
	−1.75	N	0.72	−0.81	−0.0018	0.0000		−0.0007	5.84	4.47	7.08		8.49	−0.21	0.03	0.59	
	−18.70	N	0.46	−0.62	−0.0001	0.0000		−0.0007	11.43	9.84	13.74		19.02	−0.58	0.33	−0.44	
SESAME 06 May 79	−1.28	S	−1.31	3.89	−0.0426	0.0000		−0.0058	4.18	4.43	4.00		4.68	−0.17	−0.17	−0.40	
	−0.50	N	−1.65	5.08	−0.0838	−0.0007		−0.0060	4.14	4.06	4.27		20.36	−0.22	−0.19	−0.76	
	−0.09	N	−0.79	6.25	−0.1514	−0.0024		−0.0030	4.12	3.88	4.64		4.59	−0.25	−0.24	0.19	
	0.67	S	2.66	7.65	−0.1375	−0.0008		0.0208	4.49	4.54	4.29		9.65	−0.34	−0.09	0.95	
HAPEX 19 May 86	12.87	W	−2.64	3.32	0.12	−0.20	0.08	0.14	6.04	6.38	6.58	20.11	18.16	−0.37	0.05	0.56	−0.20
	17.14	E	−2.83	2.75	0.12	−0.21	0.10	0.17	5.25	5.78	6.30	14.87	15.10	−0.31	0.10	0.63	−0.02
	24.55	W	−2.40	2.33	0.12	−0.16	0.10	0.17	5.08	6.33	5.87	12.39	18.92	−0.32	0.02	0.50	−0.15
	38.68	E	−2.31	2.15	0.09	−0.13	0.08	0.17	5.43	5.86	6.02	17.12	17.80	−0.39	0.05	0.49	0.02
	23.65	W	−2.18	2.34	0.09	−0.22	0.09	0.18	5.26	6.26	5.70	12.78	15.19	−0.30	0.06	0.63	0.06
	20.72	E	−2.04	2.43	0.16	−0.22	0.10	0.18	5.22	5.59	5.67	17.03	16.91	−0.33	0.06	0.05	−0.16

[1] The observed skewnesses of the structure function are listed in Table 2 for a separation distance of twice the sampling interval, or a separation distance of a little less than 10 m. This is the suspected maximum resolution of the data without incurring significant loss of variance due to preprocess filtering. Structure skewnesses may increase to values 20%–50% larger at separation distances of 50–100 m for some of the datasets but do not generally show universal scale dependence as is predicted for fine scale turbulence (Antonia and Van Atta 1978) or as observed in the atmospheric surface layer (Antonia et al. 1982).

HAPEX 25 May 86	37.15	W	−2.99	−1.68	0.08	0.10	0.06	0.12	5.39	6.16	6.46	24.33	18.97	−0.28	0.04	0.56	0.23
	23.85	E	−2.94	0.33	0.18	−0.08	0.06	0.14	5.54	6.06	5.96	15.99	18.91	−0.34	0.07	0.57	0.37
	40.65	W	−3.43	−0.76	0.14	0.00	0.07	0.15	5.16	5.86	6.20	20.47	16.27	−0.26	−0.01	0.29	0.20
	29.89	E	−3.66	−0.84	0.17	0.02	0.05	0.14	5.43	5.92	6.24	35.92	15.22	−0.36	0.06	0.22	0.73
	40.45	W	−2.97	0.18	0.13	0.01	0.06	0.13	5.53	6.64	6.27	35.83	18.63	−0.32	0.04	0.05	0.25
	45.22	E	−3.17	−0.50	0.11	0.07	0.07	0.13	5.25	6.78	6.05	69.91	14.73	−0.31	0.11	0.26	0.50
FIFE 6 Jun 87	6.96	E	2.10	9.42	−0.10	−0.43	0.11	0.09	4.99	5.65	6.19	11.93	12.27	−0.41	−0.10	−0.05	0.06
	8.72	W	2.03	10.28	−0.18	−0.29	0.11	0.07	5.41	6.61	5.75	12.02	12.29	−0.41	−0.20	0.27	0.37
	10.91	E	2.64	9.28	−0.11	−0.31	0.14	0.09	5.30	6.16	5.81	12.65	13.25	−0.32	0.24	0.25	0.19
	13.26	W	2.23	10.44	−0.14	−0.19	0.11	0.07	5.38	6.15	5.59	12.73	11.43	−0.49	−0.06	0.34	0.49
	9.89	E	1.51	9.65	−0.06	−0.27	0.12	0.06	4.97	5.46	5.17	11.48	9.74	−0.34	0.04	0.15	0.08
	7.39	W	1.67	10.79	−0.04	−0.31	0.11	0.06	4.66	5.78	7.16	13.46	14.01	−0.28	−0.20	0.24	0.13
HAPEX 13 Jun 86	6.91	S	1.25	−8.43	−0.12	0.57	0.07	0.16	6.52	4.76	5.86	10.47	12.60	−0.20	0.10	0.66	0.37
	13.81	S	0.74	−7.62	−0.17	0.45	0.07	0.19	6.50	6.55	6.25	12.91	15.31	−0.27	0.02	0.75	0.58
	37.44	S	1.01	−5.67	0.08	0.20	0.07	0.15	6.09	5.73	7.48	15.86	13.40	−0.35	−0.17	0.48	0.65
	19.49	W	0.13	−4.79	−0.06	0.33	0.08	0.15	5.45	8.68	6.53	17.97	14.45	−0.35	−0.12	0.01	0.28
	19.32	E	0.27	−3.28	0.05	0.31	0.07	0.13	5.65	6.27	5.69	16.64	19.41	−0.38	0.07	0.07	−0.04
	15.90	N	−0.12	−6.08	0.06	0.36	0.06	0.14	6.65	6.50	5.99	13.27	16.54	−0.34	−0.05	0.46	0.64
	11.65	N	0.06	−7.58	0.01	0.51	0.07	0.16	6.47	5.80	6.29	14.92	15.60	−0.37	0.01	0.50	0.68
HAPEX 19 Jun 86	27.28	E	−0.49	−1.25	0.13	0.04	0.07	0.11	5.05	8.55	5.68	15.62	19.75	−0.32	0.01	−0.30	0.39
	99.65	N	−1.38	−1.59	0.07	−0.03	0.09	0.14	5.39	5.53	5.05	17.49	12.62	−0.43	0.02	0.45	−0.07
	262.67	N	−0.77	−0.27	0.04	0.02	0.10	0.13	5.37	5.57	5.80	22.75	18.25	−0.35	−0.18	0.32	−0.39
	102.77	E	−0.91	0.01	−0.04	−0.08	0.09	0.16	5.73	4.64	5.59	20.33	17.66	−0.28	0.00	0.09	0.06
	425.13	W	−0.40	−0.60	0.02	−0.02	0.08	0.13	5.81	4.86	5.43	20.57	16.56	−0.35	−0.10	0.44	0.07
	41.09	S	−0.38	−2.26	0.14	0.03	0.07	0.11	6.11	4.93	5.47	12.85	13.31	−0.27	0.10	0.17	0.29
	95.69	W	−0.48	2.78	0.02	0.08	0.07	0.10	4.96	5.73	5.37	11.70	17.62	0.30	0.00	0.00	−0.31
	40.79	E	−0.67	−0.66	0.13	0.04	0.07	0.09	4.69	5.20	5.26	20.46	14.21	−0.27	0.02	−0.08	−0.06
HAPEX 22 Jun 86	14.00	E	4.16	−2.03	−0.14	0.08	0.10	0.06	6.11	6.90	5.94	21.11	16.58	−0.39	0.01	0.53	1.13
	10.67	N	3.46	−1.13	−0.25	0.03	0.11	0.09	5.48	5.25	5.43	10.93	13.71	−0.34	0.05	0.06	0.08
	5.73	N	4.78	−0.08	−0.47	0.01	0.12	0.12	5.51	5.27	5.19	13.11	11.03	−0.29	0.05	−0.08	−0.17
	4.76	S	6.25	−0.77	−0.35	−0.21	0.08	0.07	7.89	5.53	6.82	16.27	10.13	−0.47	0.45	−0.15	−0.39
	6.48	S	4.69	−2.37	−0.45	0.09	0.12	0.12	6.01	5.29	5.48	11.87	13.51	−0.28	0.06	0.26	0.24
	17.38	W	2.98	−4.18	−0.20	0.12	0.11	0.11	5.18	5.34	6.05	18.47	18.38	−0.27	0.00	0.41	0.58
	25.99	E	1.62	−1.67	−0.08	0.17	0.10	0.09	5.55	5.61	5.91	16.05	14.71	−0.31	0.02	0.76	0.70
	29.70	N	1.56	−1.40	−0.18	0.10	0.11	0.12	5.78	5.69	5.49	16.87	16.44	−0.38	−0.11	0.37	0.37
	12.73	N	4.17	−1.21	−0.44	0.10	0.12	0.18	7.37	5.59	6.33	11.29	15.45	−0.35	0.04	−0.20	0.02
HAPEX 01 Jul 86	30.93	E	−3.06	−0.26	0.09	0.09	0.06	0.09	4.98	5.54	5.91	12.25	12.95	−0.29	0.13	0.23	0.38
	22.52	N	−2.69	−1.08	0.14	0.13	0.07	0.12	5.68	4.96	5.35	11.79	12.60	−0.28	−0.06	0.00	0.13
	55.06	N	−2.43	−1.04	0.10	0.05	0.06	0.12	5.83	5.85	5.67	15.81	15.50	−0.38	0.15	0.36	0.37
	85.81	S	−0.33	−1.47	0.07	0.03	0.05	0.10	5.84	6.00	6.18	13.55	18.51	0.44	−0.15	0.84	0.46
	26.58	S	−0.57	−1.00	0.18	0.06	0.07	0.14	5.61	5.08	5.12	13.67	18.17	−0.39	−0.02	0.10	0.16
	30.33	W	−0.84	−1.54	0.14	0.07	0.07	0.12	4.85	5.41	5.24	15.38	15.52	−0.32	−0.07	0.50	0.55
	19.07	E	−2.35	−0.83	0.22	0.08	0.07	0.13	4.98	5.43	5.28	12.97	11.92	−0.26	0.17	0.14	0.18
	26.08	N	−2.58	−0.93	0.20	0.06	0.08	0.15	5.02	4.93	5.06	16.25	11.55	−0.46	−0.09	0.15	0.10
	24.83	N	−3.42	−1.02	0.16	0.13	0.08	0.14	5.69	4.91	5.35	14.40	14.35	−0.28	−0.05	−0.14	0.36
	41.76	N	−2.60	−1.42	0.12	0.10	0.06	0.15	5.52	5.79	5.68	27.85	15.27	−0.33	0.21	0.68	0.89

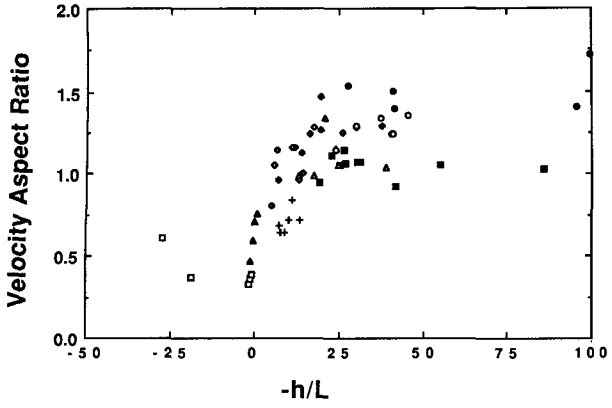

FIG. 5. The velocity aspect ratio based on the structure function (separation distance approximately 75 m) as a function of boundary-layer instability for FIFE (+), HAPEX 19 May (open triangles), 25 May (open circles), 13 June (solid diamonds), 19 June (solid circles), 22 June (open diamonds), 1 July (solid squares), and SESAME 5 May (open squares) and 6 May (solid triangles).

b. *Microfront pressure effect*

A sharp pressure maximum is often observed at or in advance of the microfront (Wilczak and Businger 1984; Schols and Wartena 1985; Shaw et al. 1990) and acts to limit the magnitude of the horizontal convergence at the microfront by accelerating the flow ahead of the front in the upstream part of the updraft and decelerating the ambient flow behind the front. This pressure effect spreads the spatial change of the longitudinal velocity component. The horizontal convergence and pressure augmentation can also be seen at the microfront from the point of view of the faster gusts penetrating downward into the surface layer and encountering slower moving updraft flow. Horizontal flow acceleration ahead of the microfronts in the slower moving drafts is inferred from analysis of aircraft data in Mahrt and Frank (1988) while the deceleration of the flow immediately behind the front and generation of secondary circulations by the "frontal pressure head" has been observed in numerous laboratory studies.

In terms of mass continuity, horizontal convergence at the surface implies updraft motion which is generated by the positive pressure perturbation and associated upward pressure gradient force. This pressure effect in the velocity variance equations assumes the form of pressure-divergence terms which in the x-direction becomes

$$p'\partial u'/\partial x < 0 \qquad (10)$$

corresponding to horizontal convergence and positive pressure perturbation in the neighborhood of the microfront. This term then corresponds to conversion of longitudinal fluctuation energy into the kinetic energy of the other two velocity components, mainly the vertical velocity component in the surface-layer turbulence studied by Schols and Wartena (1985).

Since this particular pressure effect limits the magnitude of the longitudinal convergence, but is not directly imposed on measured gradients of the flow components perpendicular to the flight path (components of fluctuating shear), the structure function variances for the two perpendicular components are significantly larger than that for the longitudinal velocity component (Table 2). While fine-scale shear instability might limit the magnitude of the fluctuating shear, such an effect is apparently not as strong as the limitation of gradients of longitudinal flow due to the spreading of the convergence zone by the implied pressure adjustments.

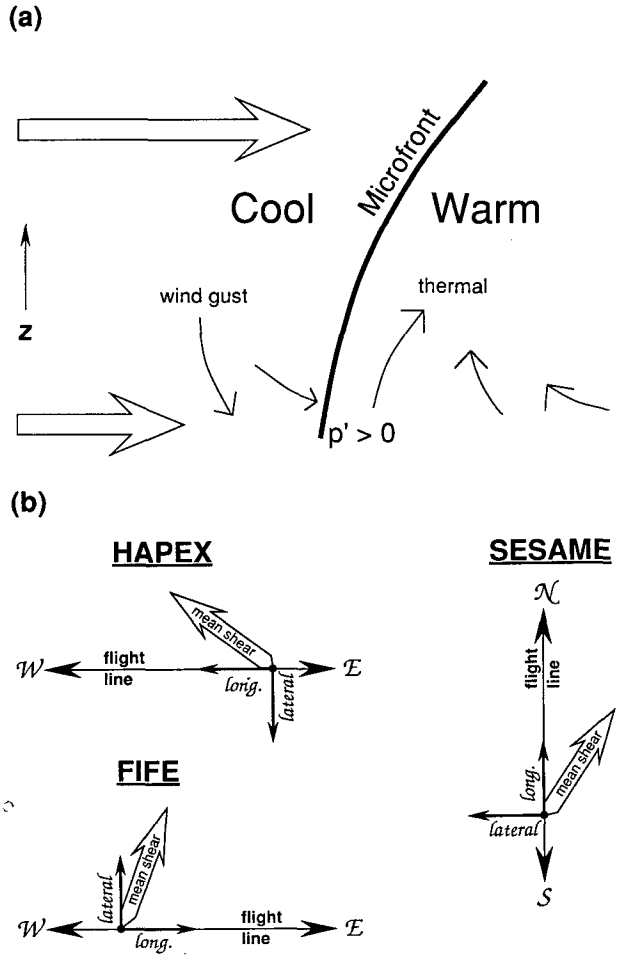

FIG. 6. (a) Plausible geometry and relative flow (small curved arrows) of asymmetric buoyant updrafts and upstream microfront in a sheared flow as inferred from the eigenfunction analysis of section 6 and the studies of Wilczak and Businger (1984) and Schols (1984). For near neutral windy conditions, the horizontal convergence at the microfront can be interpreted as descending wind gusts which impinge on slower moving air rising from the surface. In the case of strong surface heating, the convergence at the microfront can be interpreted as warm air rising into faster moving ambient air. (b) Coordinate system in the horizontal plane where the positive longitudinal flow component is defined to be in the direction of the mean shear projected onto the flight path.

Since temperature and moisture gradients are not significantly affected by pressure adjustments (shallow motion approximation) nor directly limited by shear instability, one might expect a greater likelihood for extreme gradients to occur with temperature and moisture. Indeed, the structure kurtosis for moisture and temperature is consistently larger than the kurtosis values for the velocity components. Thus, the edges of updrafts seem to be much sharper in terms of temperature and moisture compared to the velocity components consistent with previous studies (e.g., Wilczak 1984; Mahrt 1981).

c. *Relation to projected shear-buoyancy ratio*

Since the shear-induced eddy asymmetry is largest when the mean shear is largest, the structure skewness values are expected to be influenced by the values of the instability parameter $-h/L$. However, the direction of the mean shear with respect to the flight path is also important so that the Obukhov length is by itself inadequate to describe the asymmetry of the main updrafts. As an alternative, consider the ratio of the mean shear projected onto the flight direction[2] to the influence of buoyancy effects.

Using the wind itself to infer the low-level shear, the influence of mean shear on eddy asymmetry can be predicted in terms of the simple *projected shear-buoyancy ratio*

$$u_f/w^* \tag{11}$$

where w^* is the free-convection velocity scale

$$w^* = \{(g/\Theta)[w'\theta_v']h)\}^{1/3} \tag{12}$$

and u_f is the mean wind component projected onto the flight direction (negative when directed opposite to the flight direction). The SESAME cases have been omitted from these comparisons because the free-convection velocity scale is not applicable for stable stratification. When the ratio (11) is large, the shear distortion of the updrafts in the aircraft flight direction should be rapid compared to the vertical translation rate of a fluid element by the buoyancy-induced updraft speed. Since the updraft velocities are generated by both buoyancy and shear instabilities, the denominator of (11) in more complete form should be a function of both effects; however, this study continues with the simple ratio (11) for an initial qualitative study of the mean shear effect.

The shear instability ratio u_f/w^* does indeed normally predict the sign of the projected structure skewness of temperature and appears to account for some of the variation of the skewness magnitude although the scatter is large (Fig. 7). When the longitudinal flow is significant so that $u_f/w^* > 1$, the direction of the longitudinal flow determines the sign of the skewness for temperature gradients in all cases except one. Nonetheless, significant scatter remains. This scatter is probably related to sampling problems, various orientations of the mean shear with respect to the flight direction, height dependence of the mean shear, and other physical influences not contained in u_f/w^*. The skewness of moisture and vertical velocity gradients (not shown) are also influenced by the flow parallel to the flight direction u_f, although the correlation appears to be smaller than that for temperature probably for reasons discussed in subsection a.

The skewness of the longitudinal velocity component gradients (Fig. 8) is also controlled by the direction of the longitudinal flow with respect to the flight direction in a way consistent with the expected formation of the strongest gradients (convergence) at the upstream edges of the updrafts. For example, when the longitudinal flow component is directed in the same direction of the aircraft ($u_f > 0$), the projected structure skewness of the longitudinal flow component is almost always negative corresponding to narrow zones of strong horizontal convergence and broader regions of horizontal divergence. Conversely, the projected skewness for the longitudinal flow is generally positive when the longitudinal flow is directed opposite to the flight direction in agreement with the microfront prediction. Note that the skewness of the convergence always exceeds a minimum magnitude of 0.2 suggesting that significant convergence always occurs at the upstream boundary even with weak shear. The convergence is a self-intensifying frontogenesis process so that weak convergence concentrates the horizontal gradient of the longitudinal flow, and thus further intensifies the frontogenesis process. The fact that the convergence effect does not increase significantly with further increases of mean shear may suggest some negative feedback or limiting process, such as pressure effects and fine-scale shear instability.

5. Horizontal scale

The important horizontal scales can be qualitatively posed in terms of wavelet phase plots with the horizontal scale (transformation window width) as the vertical axis and spatial position within the record as the horizontal axis (Fig. 3). However, interpretation of such phase plots may depend on preconceived notions of the interpreter. Furthermore, it is not practical to carry out interpretation of phase plots for all of the records.

Therefore, this study departs from the usual wavelet phase plots and constructs "global" statistics of the wavelet transform as discussed in section 2. The variance of the Haar-wavelet transform of vertical velocity

[2] With this projection, the structure skewness is simply the skewness of subsection a multiplied by the sign of the projected horizontal flow u_f where $u_f > 0$ when the horizontal flow is in the same direction as the aircraft flight and $u_f < 0$ when the horizontal flow is in the opposite direction to the aircraft flight. This projection is used only in this subsection to spread the skewnesses to either sign for purposes of visualization.

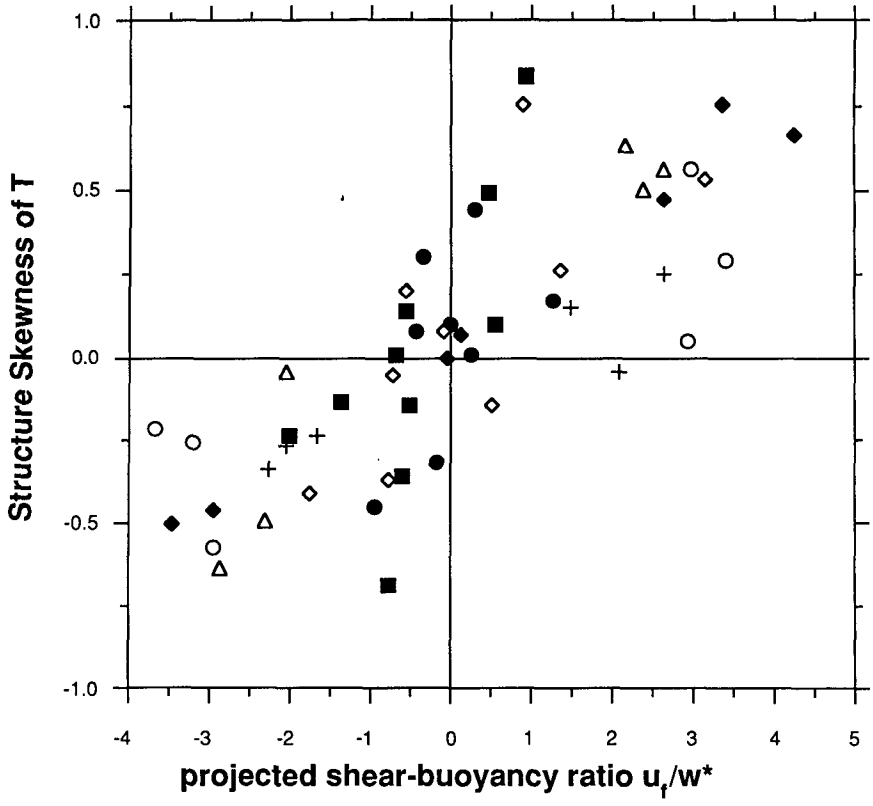

FIG. 7. Structure skewness of temperature with respect to gradients projected onto the flight direction (10-m separation distance) as a function of the projected shear-buoyancy ratio u_f/w^*. Symbols as in Fig. 5.

is computed for the long HAPEX flights over the forest (19 and 25 May) since these two datasets contain the largest sample size. For 19 May, the Haar-wavelet variance for vertical velocity (Fig. 9) shows a peak at horizontal scales between 300 and 400 m with an rms velocity fluctuation of about 0.5 m s^{-1}. Recall that the peak of the Haar-wavelet spectra measures the spatial coherence of changes corresponding to roughly twice the width of the updraft. The corresponding structure function (Fig. 9) leads to similar conclusions if one defines the dominant scale indirectly in terms of the decrease of the slope of the structure function with increasing separation distance. The structure function does not directly isolate the main eddy scale as demonstrated in section 2. Power spectra of the vertical velocity (not shown) show a diffuse maximum at about 1.2 km which corresponds to the periodicity of the updrafts. This 1.2-km wavelength includes the spacing between the updrafts.

The peak of the variance for temperature corresponds to a rms temperature perturbation on the order of 0.1°C and occurs at a little larger scale than the peak for vertical velocity. The Haar-wavelet variance of the lateral velocity component (horizontal flow perpendicular to the flight path) indicates a maximum at a little less than 200 m. The analysis of section 6 indicates that this shear is associated with vorticity in the vicinity of the microfronts.

For 19 May, the wavelet skewness for temperature and vertical motion reach a positive peak at horizontal scales a little smaller than 100 m (Fig. 10b) with a negative peak of the skewness of the longitudinal component u occurring at 400–500 m. These signs agree with the expected influence of mean shear on eddy asymmetry and formation of microfronts (Fig. 6a). However, the wavelet skewness represents the net difference between the influences of the microfronts and the opposing influence of the more diffuse downstream gradients, and is also affected by the influence of the fine scale turbulence on the scale dependence of the variance occurring in the denominator of the skewness. As a result, the exact scale of the skewness peak has no easily defined interpretation and the conclusions must be limited to the overall sign of the skewness at smaller scales and implied eddy asymmetry. However, note that the gradient skewnesses for temperature and the longitudinal component are greater than that for vertical velocity in agreement with subsection a.

The scale dependencies on 25 May (Fig. 11) are similar to those of 19 May except that the dominant

scales are shifted to larger horizontal scales. This shift is probably related to the somewhat higher flight elevation on 25 May (Table 1) and related to the orientation of the mean shear more parallel to the flight track on this day.

6. Eddy structure and transport

a. Correlation Prandtl number and momentum flux

With significant heating, the correlations between the horizontal velocity components and the vertical motion is generally quite weak, about 0.1 or less. In contrast, for the two cases of strongest wind shear (SESAME 6 and FIFE), the correlation between vertical velocity and the horizontal velocity component most aligned with the shear is a little more than 0.3 (Table 2). The decrease of the correlation between the vertical and horizontal velocity components with increasing instability is predicted by surface layer similarity theory (Kaimal et al. 1972) and is observed in the convective surface layer studied by Wilczak 1984). In contrast, the correlation between temperature and vertical velocity increases slightly with increasing instability as is also observed by Kaimal et al. (1972) and Wilczak (1984).

The collective effect of these two statistical tendencies can be combined by defining a correlation Prandtl number

$$P = [(r_{wu})^2 + (r_{wv})^2]^{1/2}/r_{wT}$$

where r is the correlation coefficient. As expected, the correlation Prandtl number decreases with increasing instability (Fig. 12) verifying the inefficiency of the momentum transport by buoyant updrafts.

Zilitinkevich (1973) argues that for sufficient instability, the mechanical production of horizontal velocity fluctuations does not lead to significant vertical velocities. The vertical velocities are instead controlled by buoyancy. Similarly, McBean (1974) argues that in the unstable case the vertical velocity fluctuations are driven primarily by buoyancy and become *almost random* with respect to the horizontal velocity fluctuations. The lack of interaction between the shear-generated horizontal velocity fluctuations and thermals might also be inferred from the close relationship between vertical velocity skewness and the free convection velocity scale observed in Hunt et al. (1988). The skewness seemed to be independent of the friction velocity even when the shear generation of turbulence was the same order as the buoyancy-produced turbulence.

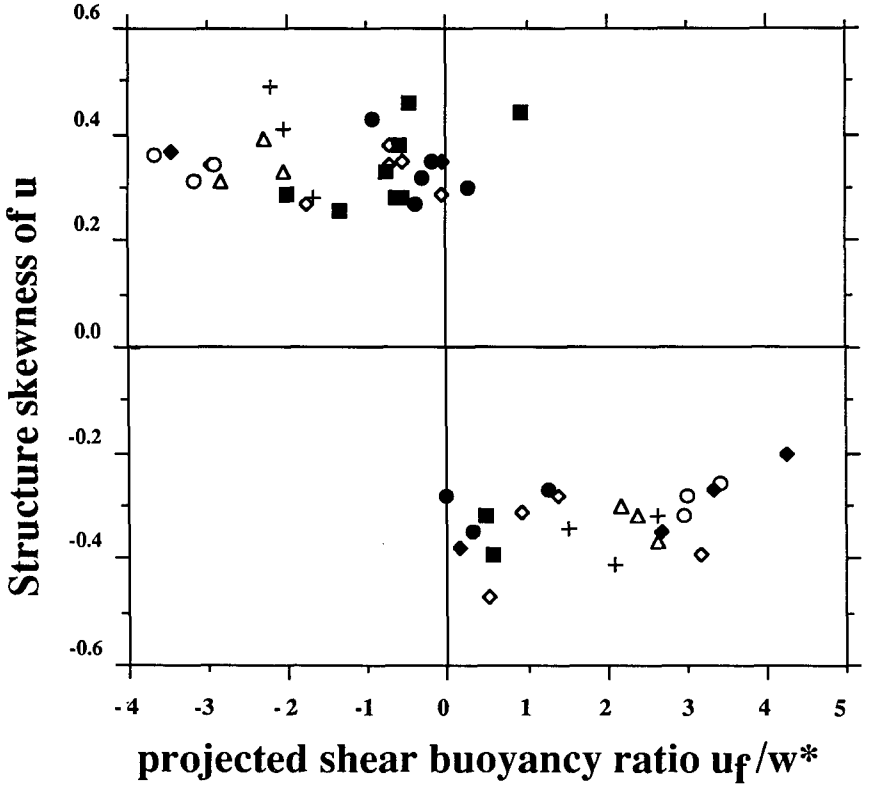

FIG. 8. Structure skewness of the longitudinal velocity component with respect to gradients projected onto the flight direction (10-m separation distance) as a function of the projected shear–buoyancy ratio u_f/w^*. Symbols as in Fig. 5.

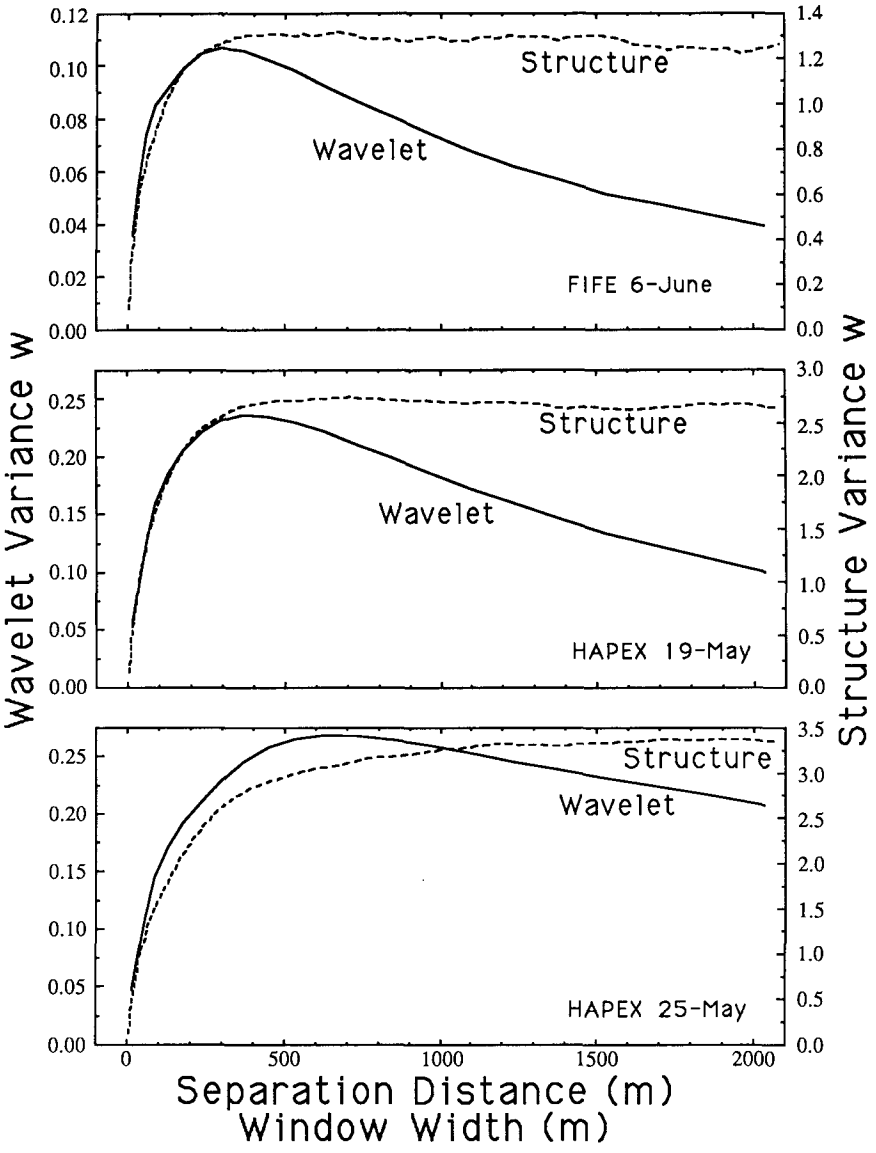

FIG. 9. Statistics of the vertical velocity structure function and Haar-wavelet variance for vertical velocity as a function of separation distance and window width L', respectively, as composited over the flight legs for 19 and 25 May of HAPEX.

The present study will suggest that with significant convective instability, the correlation between the horizontal velocity and vertical velocity components is reduced by *systematic* phase differences between the horizontal velocity component and the buoyancy-generated vertical motion rather than by random phase differences. In other words, as the surface heating becomes stronger and the mean shear weaker, the horizontal convergence becomes more centered (inphase) with respect to the thermals so that u and w are more out-of-phase.

In contrast, with no surface heating, the fluctuations of horizontal velocity are generated by vertical motions acting on the mean shear as assumed in mixing length theory. This vertical advection by the fluctuating vertical motion leads to significant correlation between horizontal and vertical velocity fluctuations. With no other influences, the strongest gradient of horizontal momentum is expected at the upstream microfront boundary between the sinking ambient flow with strong horizontal motion and the updraft with slower horizontal motion. This corresponds to an inphase relationship between the vertical velocity and the horizontal velocity components. Such geometry is observed by Schols (1984) for the case of weak surface heating and sketched in Stull (1988, Section 11.1.2).

In some circumstances, the above conceptual view requires modification due to pressure fluctuations. Sinking motion with stronger horizontal momentum generates positive perturbation pressure at or in advance of its leading edge. This leading edge is the microfront boundary between the sinking motion and slower moving updraft air (Wilczak 1984; Shaw et al. 1990; see Fig. 6a above). The positive pressure perturbation in turn horizontally accelerates the flow in the upstream part of the updraft as discussed in section 4. As a result, the maximum horizontal convergence appears to be shifted to inside the updraft between the microfront edge and updraft center (Wilczak 1984). The exact location of the maximum convergence is probably influenced by both the microfront positive pressure perturbation and low pressure in the center of the updraft (Wilczak and Businger 1984) where the latter may be associated with buoyancy induced upward acceleration. Because of the influence of vertical advection on the horizontal convergence, a simple relationship between the pressure field and horizontal convergence is not possible.

As a result of pressure effects, the horizontal velocity is somewhat out-of-phase with the vertical motion while the temperature and vertical motion remain approximately inphase as long as buoyancy is of some

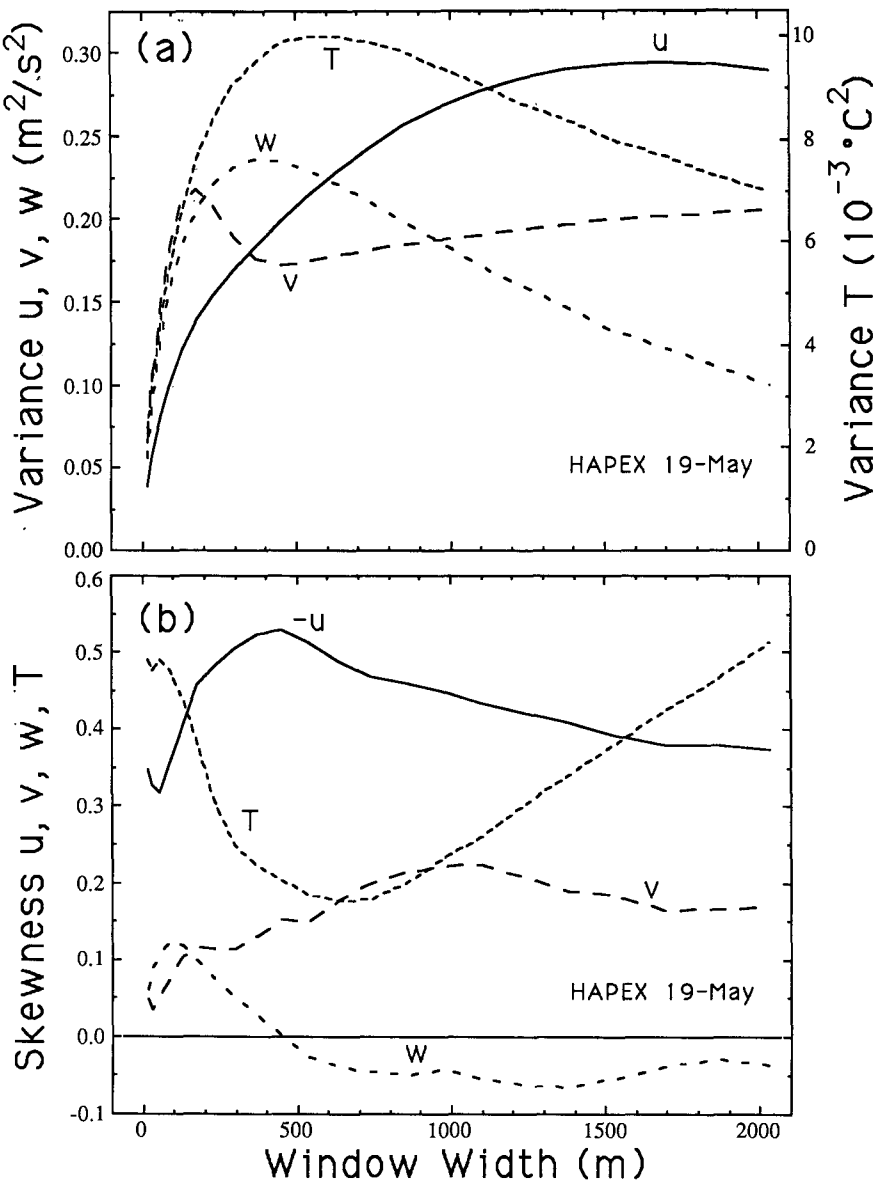

FIG. 10. Dependence of the Haar-wavelet variance (a) and skewness (b) on horizontal scale as composited over the flight legs for HAPEX 19 May. For compactness, the skewness of $-u$ is plotted.

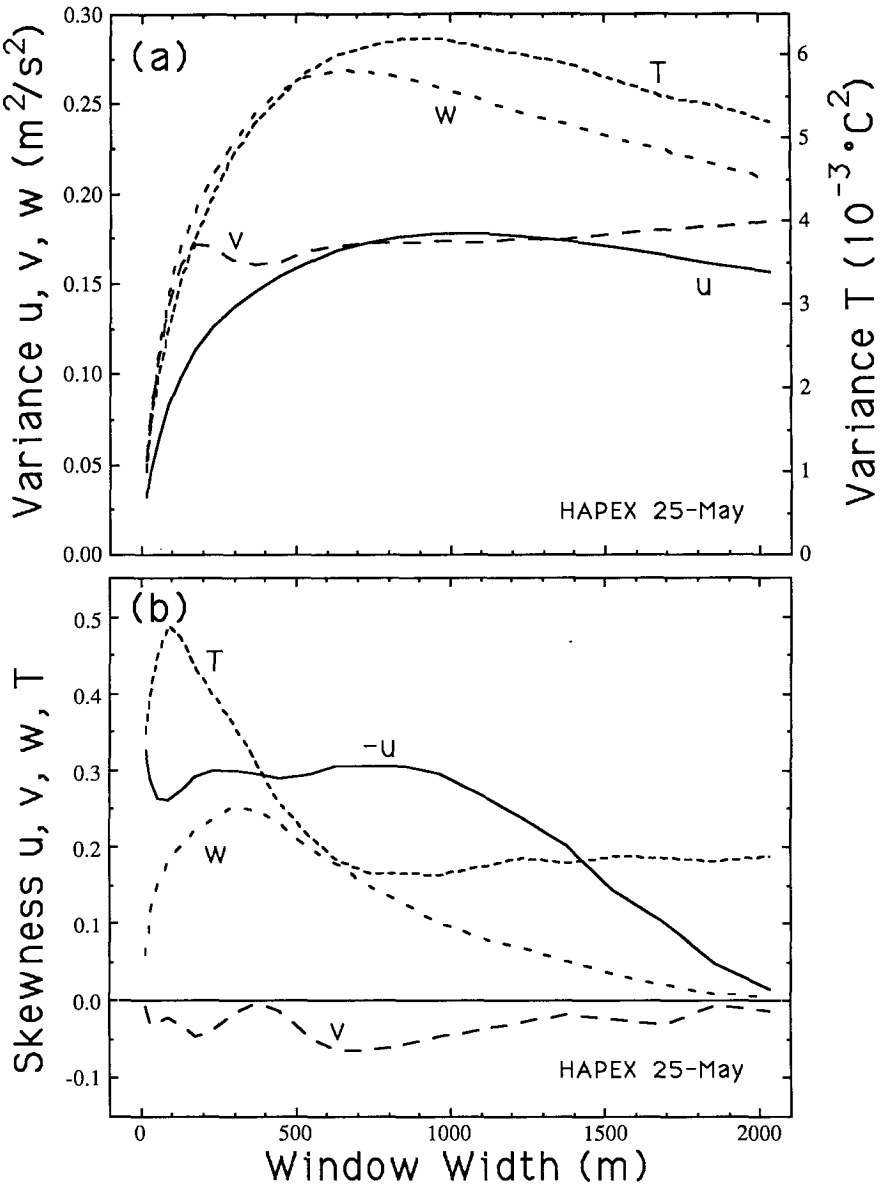

FIG. 11. Dependence of the Haar-wavelet variance and skewness on scale as composited over the flight legs for HAPEX 25 May. For compactness, the skewness of $-u$ is plotted.

significance. Then the correlation Prandtl number is less than one, at least for the data analyzed here. The phase shift between horizontal velocity and vertical motion corresponds to reduced net momentum flux for the updraft, which can be associated with subregions of countergradient momentum flux in composited sheared thermals (Antonia and Chambers 1978; Wilczak 1984).

From the point of view of the updraft bulk motion, the positive pressure perturbation near the convergent updraft edge corresponds to a horizontal pressure difference across the updraft. This pressure gradient horizontally accelerates the draft which reduces the horizontal velocity deficit of the updraft (Mahrt 1981). This in turn reduces the vertical transport of horizontal momentum. This notion can be rephrased in terms of smaller mixing length for momentum due to horizontal acceleration of slower moving parcels by the fluctuating horizontal pressure gradient. This reduction of momentum mixing could account for the observation that momentum is often not well mixed even in boundary layers which are well mixed in mean potential temperature. This is indeed the case for many of the boundary layers studied here. Note that this limitation of the momentum flux is posed in terms of reduced amplitude of the average horizontal momentum deficit

of the updrafts, whereas the previous paragraphs emphasized the phase lag between the velocity components.

b. Eigenstructure of the updrafts

The structure of the most coherent events observed in FIFE and observed in the long aircraft records 150 m above the pine forest in HAPEX are now studied. These are the most homogeneous cases. Toward this goal, the eigenvectors of the multivariate correlation matrix based on samples selected in terms of the Haar-wavelet transform of vertical velocity are computed according to the procedure outlined in Mahrt and Frank (1988) and briefly discussed in section 2d. With this approach, samples are selected with sharp spatial changes of vertical velocity centered within the samples. The sample width L' is chosen to be 600 m to include the peak of the Haar-wavelet variance for vertical velocity for all datasets. Samples were selected according to horizontal changes of vertical motion instead of temperature or moisture to ensure capture of active updrafts. Using the procedure outlined in section 2d, approximately 500 samples are selected for both HAPEX 19 and 25 May and 131 samples for the FIFE data representing between 40% and 50% of the total record.

The most important (first) eigenvector indicates that the maximum horizontal convergence is indeed between the microfront edge and the center of the buoyant updraft for both HAPEX days (Fig. 13), consistent with the observations of Wilczak (1984) near the top of the 130-m tower layer. Notice that the change of temperature at the microfront is quite concentrated and inphase with the vertical velocity while the spatial changes of the horizontal velocity components are more diffuse, consistent with the role of pressure fluctuations on the velocity components discussed in section 4. The horizontal change of vertical velocity at the microfront is sharper than the other variables because the sampling procedure is based on vertical velocity.

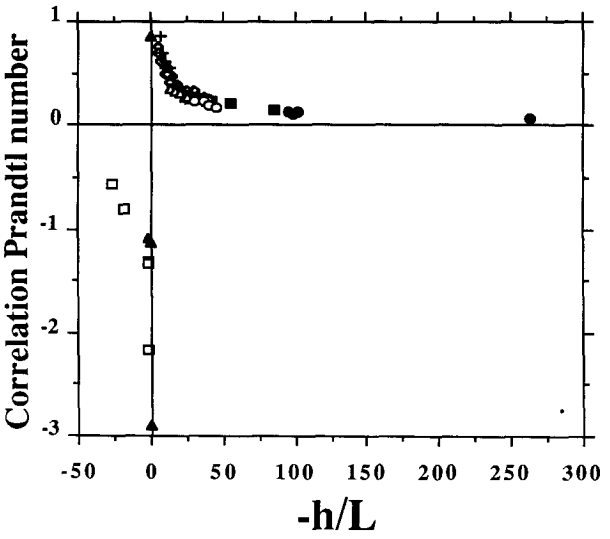

FIG. 12. The correlation Prandtl number as a function of boundary-layer instability for FIFE (+), HAPEX 19 May (open triangles), 25 May (open circles), 13 June (solid diamonds) 19 June (solid circles), 22 June (open diamonds), 1 July (solid squares), and SESAME 5 May (open squares) and 6 May (solid triangles).

In the FIFE case where the shear is more perpendicular to the flight path, the observed horizontal convergence is more centered with respect to the updraft as also observed by Wilczak (1984) for the flow component perpendicular to the wind. In the direction perpendicular to the mean shear, there is no mechanism to generate systematic asymmetry in a preferred direction. In fact, the extension of the horizontal convergence inward from the microfront in the HAPEX 19 May case might be enhanced by inclusion of some of the convergence perpendicular to the mean shear because the mean shear is not completely aligned with the flight direction on this day. The three influences that extend the horizontal convergence from the upstream microfront to the center of the updraft can now be summarized as 1) buoyancy, 2) pressure adjustments, and 3) horizontal convergence of the flow perpendicular to the mean shear.

For each of the three days (Fig. 13), the first eigenvector explains 25%–30% of the variance. This percentage is typical of turbulent flows where a variety of types of motions coexist. The second eigenvector explains only 5%–10% of the variance, and when added to the first eigenvector augments or reduces horizontal convergence at the microfront (expansion coefficient[3] occurs with either sign). Higher-order eigenvectors correspond to progressively smaller scales with more chaotic patterns especially in FIFE where the sample size is smaller.

For HAPEX 19 May, significant shear of the lateral velocity component occurs within the buoyant updraft in a 150-m zone adjacent to the microfront corresponding to the scale of the relative maximum of the Haar-wavelet variance for the lateral velocity component (Fig. 10a). Taking into account the direction of the mean shear (Fig. 9b) and the fact that the samples are demeaned, the first eigenvector indicates weaker lateral momentum in the buoyant updraft, which is probably related to upward advection of weaker momentum. Such shear of the lateral component does not systematically occur in connection with the buoyant updraft of the first eigenvector for 25 May, presumably because the mean flow is directed more parallel to the flight path on that day.

[3] The expansion coefficient is the projection of the observational vector of the sample onto the eigenvector (see Panofsky and Dutton 1984, chapter 12.5).

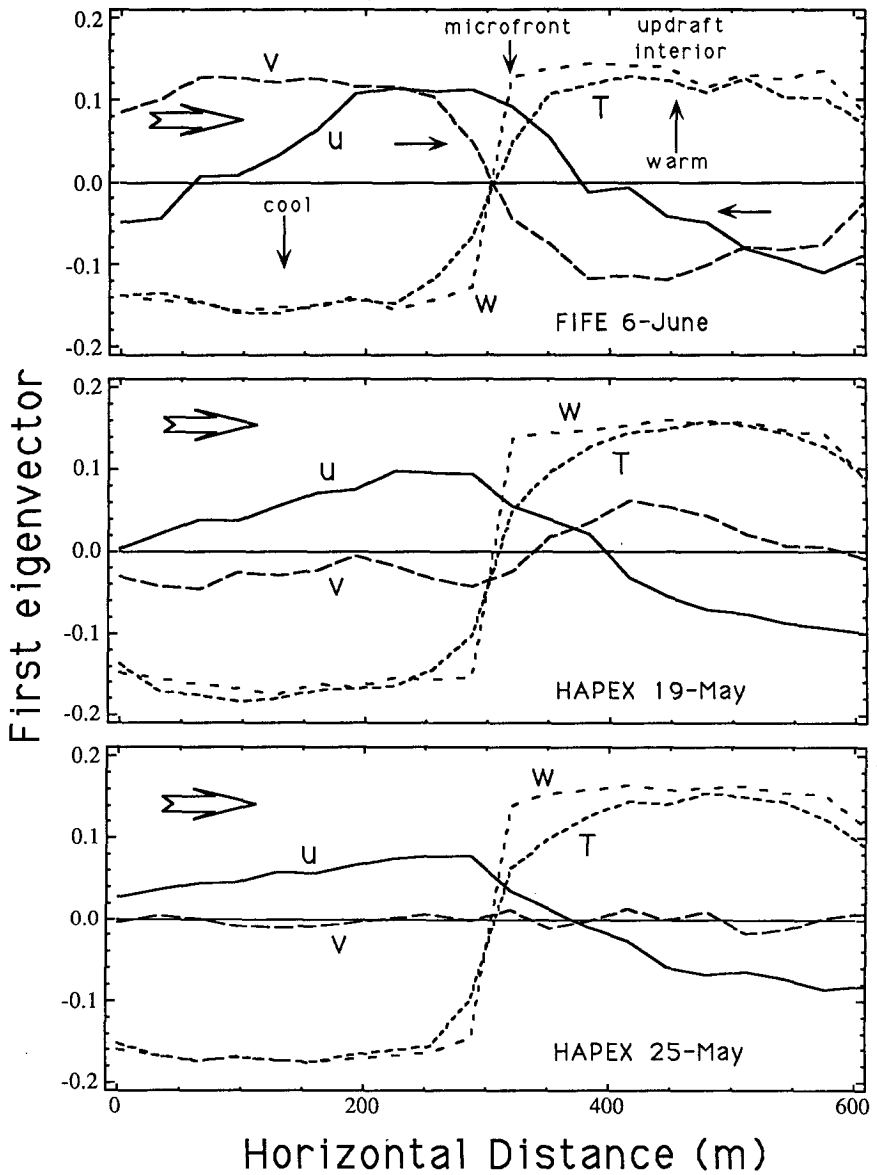

FIG. 13. The leading eigenvector of the lagged correlation matrix for conditionally sampled sharp horizontal changes of vertical velocity for HAPEX 19 and 25 May and FIFE. The coordinate system is sketched in Fig. 6b. The eigenvector calculation yields demeaned nondimensional variables which are scaled such that the total magnitude of the eigenvector is unity.

The first eigenvector of the FIFE case contains strong shear of the lateral component in a 150–200 m zone centered about the microfront. This width is approximately the scale of the relative maximum of the Haar-wavelet variance of the lateral velocity component. This horizontal shear of the lateral component corresponds to warm updrafts with weak southerly flow and sinking cooler air with strong southerly flow which is expected from simple vertical advection. In other terms, gradients of the lateral component (vorticity) are generated by horizontal gradients of eddy vertical velocity acting on the mean shear. This tilting mechanism is distinctly different from the intensification of vorticity due to vortex stretching by vertical acceleration in the buoyancy updrafts (Kaimal and Businger 1970).

The horizontal wind speed is greatest just upstream from the microfront for all three datasets, as can be shown by combining the mean values with the perturbation structures inferred from Fig. 13. The resulting sharp decrease of wind speed in the flow direction at the microfront can be viewed as the leading edge of a descending wind gust consistent with the interpretation of Schols (1984) and Shaw et al. (1990). The gust point-of-view is particularly useful in cases of stronger

shear and weaker surface heating (smaller $-h/L$) where the correlations between temperature and horizontal velocity components are larger (Table 2). With strong shear, temperature becomes more of a tracer controlled by vertical advection of shear-driven motion and less responsible for generation of vertical motions.

Qualitatively similar results are obtained if temperature or lateral velocity are used instead of vertical velocity to select the samples. The results are not sensitive to the choice of the window width for variations up to about a factor of two. One exception is that the third eigenvector for the FIFE case may capture a mode where warm air sinks toward the surface and cool air is rising; apparently related to the second phase of shear-driven overturning similar to that observed in Mahrt (1985) and Mahrt and Frank (1988).

7. Conclusions

The above data analysis indicates that the variance spectra of the Haar-wavelet transform is superior to the structure function for identifying the most important scales of spatial variation, as analytically predicted in section 2. The wavelet skewness spectra are able to quantify the asymmetry of the main eddies due to mean shear. Finally, the internal eddy structure has been studied using eigenvectors of the lagged correlation matrix for structures conditionally sampled in terms of the Haar-wavelet transform. This technique finds asymmetric updrafts bounded by a microfront zone of strong horizontal changes at the upstream edge. This microfront zone is generated by horizontal convergence between the faster horizontal motion of the descending air and the slower horizontal motion of the updraft.

The momentum flux depends on the nature of this updraft asymmetry through a phase shift between the vertical and horizontal velocity fluctuations. In a theoretical regime dominated by eddy-vertical advection in the presence of mean shear, the change of horizontal momentum occurs mainly at the upstream edge of the updraft leading to high correlation between the velocity components and efficient vertical transport of horizontal momentum. However, two additional factors affect the eddy horizontal wind field. First, a pressure maximum is generated at or in advance of the upstream microfront (Wilczak, 1984; Wilczak and Businger 1984; Schols 1984; Shaw et al. 1990). The corresponding pressure gradient accelerates the flow just inside the updraft (downwind from the microfront). This spreads the horizontal convergence inward from the microfront. Second, buoyancy effects tend to generate horizontal convergence in the center of the updraft. In fact, the convergence field is expected to be symmetric with respect to the buoyant updraft in the limiting case of vanishing mean shear. These effects lead to a phase shift between the horizontal and vertical velocity components so that the center of the horizontal convergence is shifted from the upstream microfront into the region between the microfront and the updraft center (section 6).

As a result, the correlation between the vertical and horizontal velocity components decreases with increasing surface heating and decreasing mean shear. Thus, the efficiency of the momentum flux and the correlation Prandtl number decrease with increasing boundary-layer instability ($-h/L$). That is, *the systematic phase lag between the horizontal and vertical velocity components in heated conditions may explain the partial decorrelation between the horizontal and vertical velocity components previously attributed to randomness.* This eddy model may be useful in estimating the behavior of the momentum mixing through the boundary layer in recognition of the observation that momentum is often not well mixed even when mean potential temperature is almost constant with height.

The above conceptual model is supported by the statistics of fluctuating gradients based on the usual structure functions and the Haar-wavelet transform. The positive pressure perturbation associated with the microfront is thought to "spread" the horizontal convergence. This contention is consistent with the observed weaker horizontal gradients of the longitudinal flow compared to the horizontal gradients of the lateral and vertical velocity components. However, the horizontal gradients of the longitudinal flow exhibit strong skewness which corresponds to concentrated convergence at the upstream microfronts. Finally, the spatial changes of temperature and moisture are much sharper than the velocity gradients because they are not directly affected by pressure effects nor by small-scale shear instability.

Acknowledgments. The comments of Nimal Gamage, Jin-Won Kim, C. W. Van Atta, the reviewers, and the computational and graphics assistance of Wayne Gibson, Jacob Jensen, and Kristin Mahrt are greatly appreciated. The Computer Services Division of the National Center for Atmospheric Research is acknowledged for computational support and the Research Aircraft Facility of the same institution is acknowledged for the aircraft data listed in Table 1 with special appreciation to Dick Friesen. This material is based upon work supported by the Physical Meteorology and Mesoscale Meteorology Programs of the National Science Foundation under Grants ATM-8521349 and ATM-8820090, respectively.

REFERENCES

André, J. C., and collaborators, 1988: HAPEX-MOBIHLY. First results from the special observing period. *Ann. Geophys.*, **6**, 477–492.

Antonia, R. A., and A. J. Chambers, 1978: Note on the temperature ramp structure in the marine surface layer. *Bound.-Layer Meteor.*, **15**, 347–355.

——, ——, and E. F. Bradley, 1982: Relationships between structure

functions and temperature ramps in the atmospheric surface layer. *Bound.-Layer Meteor.*, **23**, 395–403.
——, and J. D. Atkinson, 1976: A ramp model for turbulent temperature fluctuations. *Phys. Fluids*, **19**, 1273–1278.
——, and C. W. Van Atta, 1978: Structure functions of temperature fluctuations in turbulent shear flows. *J. Fluid. Mech.*, **84**, 561–580.
Argoul, F., A. Arneodo, G. Grasseau, Y. Gagne, E. J. Hopfinger and U. Frisch, 1989: Wavelet analysis of turbulence reveals the multifractal nature of the Richardson cascade. *Nature*, **338**, 51–53.
Babiano, A., C. Basedevant and R. Sodourney, 1985: Structure functions and dispersion laws in two-dimensional turbulence. *J. Atmos. Sci.*, **42**, 941–949.
Bergström, H. and U. Högström, 1989: Turbulent exchange above a pine forest. Part II. Organized structures. *Bound.-Layer Meteor.*, **49**, 231–163.
Busch, N., and E. L. Petersen, 1971: Analysis of nonstationary ensembles. *Statistical Methods and Instrumentation on Geophysics*. A. G. Kjelass, Ed., Teknologisk Forlag, 71–92.
Chen, C. H. P., and R. F. Blackwelder, 1978: Large-scale motion in turbulent boundary layer: A study using temperature contamination. *J. Fluid Mech.*, **89**, 1–31.
Daubechies, Ingrid, 1988: Orthonormal bases of compactly supported wavelets. *Commun. Pure and Appl. Math.*, **61**, 909–996.
Frisch, U., P. L. Sulem and M. Nelkin, 1978: A simple dynamical model of intermittent fully developed turbulence. *J. Fluid Mech.*, **87**, 719–736.
Gao, W., R. H. Shaw, and K. T. Pau U, 1989: Observation of organized structure in turbulent flow within and above a forest canopy. *Bound.-Layer Meteor.*, **47**, 349–378.
Greenhut, G. K., and S. J. S. Khalsa, 1982: Updraft and downdraft events in the atmospheric boundary layer over the equatorial Pacific Ocean. *J. Atmos. Sci.*, **39**, 1803–1818.
Grossman, R. L., 1982: An analysis of vertical velocity spectra obtained in the BOMEX fair-weather, trade-wind boundary layer. *Bound.-Layer Meteor.*, **23**, 323–357.
Grossmann, A., R. Kronland-Martinet and J. Morlet, 1989: Reading and understanding continuous wavelet transforms. *Wavelets*, J. M. Combes, A. Grossmann, and Ph. Tchamitchian, Eds., Springer Verlag, 315 pp.
Hunt, J. C. R., J. C. Kaimal and J. E. Gaynor, 1988: Eddy structure in the convective boundary layer; new measurements and concepts. *Quart. J. Roy. Meteor. Soc.*, **114**, 827–858.
Kaimal, J. C., and J. A. Businger, 1970: Case studies of a convective plume and a dust devil. *J. Appl. Meteor.*, **9**, 612–620.
——, J. C. Wyngaard, D. A. Haugen, O. R. Cote and Y. Izumi, 1972: Spectral characteristics of surface-layer turbulence. *Quart. J. Roy. Meteor. Soc.*, **98**, 563–589.
Kikuchi, T., and O. Chiba, 1985: Steplike temperature fluctuations associated with inverted ramps in a stable surface layer. *Bound.-Layer Meteor.*, **31**, 51–63.
Lenschow, D. H., 1970: Airplane measurements of planetary boundary layer structure. *J. Appl. Meteor.*, **9**, 874–884.
——, X. S. Li, C. J. Zhu and B. B. Stankov, 1988: The stably stratified boundary layer over the great plains. Part II: Horizontal variations and spectra. *Bound.-Layer Meteor.*, **42**, 123–135.
Lumley, J. L., 1970: *Stochastic Tools in Turbulence*. Academic Press, 194 pp.
——, and H. A. Panofsky, 1964: *The Structure of Atmospheric Turbulence*. Wiley Interscience, 239 pp.
Mahrt, L., 1981: Circulations in a sheared inversion layer at the mixed layer top. *J. Meteor. Soc. Japan*, **59**, 238–241.
——, 1985: Vertical structure and turbulence in the very stable boundary layer. *J. Atmos. Sci.*, **42**, 2333–2349.
——, 1989: Intermittency of atmospheric turbulence. *J. Atmos. Sci.*, **27**, 79–95.
——, 1991: Boundary-layer moisture regimes. *Quart. J. Roy. Meteor. Soc.*, **117**, submitted.
——, and N. Gamage, 1987: Observations of turbulence in stratified flow. *J. Atmos. Sci.*, **44**, 1106–1121.
——, and H. Frank, 1988: Eigenstructure of eddy microfronts. *Tellus*, **40A**, 107–119.
McBean, G. A., 1974: Turbulent transfer mechanisms. *Quart. J. Roy. Meteor. Soc.*, **100**, 53–66.
Meyer, Y., 1989: Orthonormal wavelets. *Wavelets*. J. M. Combes, A. Grossmann, and Ph. Tchamitchian, Eds., Springer Verlag, 315 pp.
Nicholls, S., 1978: Measurements of turbulence by an instrumented aircraft in a convective atmospheric boundary layer over the sea. *Quart. J. Roy. Meteor. Soc.*, **104**, 653–676.
Noilhan, J., and S. Planton, 1989: A simple parameterization of land surface processes for meteorological models. *Mon. Wea. Rev.*, **117**, 536–549.
Panofsky, Hans A., and John A. Dutton, 1984: *Atmospheric Turbulence*. John Wiley and Sons, 397 pp.
Petersen, E. L., 1976: A model for the simulation of atmospheric turbulence. *J. Appl. Meteor.*, **15**, 571–578.
Pinty, J. P., P. Mascart, E. Richard and R. Rosset, 1989: An investigation of mesoscale flows induced by vegetation inhomogeneities using an evapotranspiration model calibrated against HAPEX-MOBILHY data. *J. Appl. Meteor.*, **28**, 976–992.
Schols, J. L. J., 1984: The detection and measurement of turbulent structures in the atmospheric surface layer. *Bound.-Layer Meteor.*, **29**, 39–58.
——, and L. Wartena, 1985: A dynamical description of turbulent structures in the near neutral atmospheric surface layer: The role of static pressure fluctuations. *Bound.-Layer Meteor.*, **34**, 1–15.
Sellers, P. J., F. J. Hall, G. Asrar, D. E. Strebel and R. E. Murphy, 1988: The first ISLSCP Field Experiment (FIFE). *Bull. Amer. Meteor. Soc.*, **69**, 22–27.
Sirovich, L., 1987: Turbulence and the dynamics of coherent structures. Part I: Coherent structures. *Quart. Appl. Math.*, **45**, 561–571.
Shaw, R. H., K. T. Paw U, X. J. Zhang, W. Gao, G. Den Hartog and H. H. Neumann, 1990. Retrieval of turbulent pressure fluctuations at the ground surface beneath a forest. *Bound.-Layer Meteor.*, **50**, 319–338.
Stull, R. B., 1988: *An Introduction to Boundary Layer Meteorology*. Kluwer Academic, 666 pp.
Tennekes, H., and J. C. Wyngaard, 1972: The intermittent small-scale structure of turbulence: data processing hazards. *J. Fluid Mech.*, **55**, 93–103.
Van Atta, C. W., 1977: Effect of coherent structures on structure functions of temperature in the atmospheric boundary layer. *Arch. Mech.*, **29**, 161–171.
Wilczak, J. M., 1984: Large-scale eddies in the unstably stratified atmospheric surface layer. Part 1: Velocity and temperature structure. *J. Atmos. Sci.*, **24**, 3537–3550.
——, and J. E. Tillman, 1980: The three-dimensional structure of convection in the atmospheric surface layer. *J. Atmos. Sci.*, **37**, 2424–2443.
——, and J. A. Businger, 1984: Large-scale eddies in the unstably stratified atmospheric surface layer. Part II: Turbulent pressure fluctuations and the budgets of heat flux, stress and turbulent kinetic energy. *J. Atmos. Sci.*, **24**, 3551–3567.
Zilitinkevich, S. S., 1973: Shear convection. *Bound.-Layer Meteor.*, **3**, 416–423.